Simulation of 100–300 GHz Solid-State Harmonic Sources

Michael F. Zybura, J. Robert Jones, *Student Member, IEEE,* Stephen H. Jones, *Member, IEEE,* and Gregory B. Tait, *Member, IEEE*

***Abstract*—Accurate and efficient simulations of the large-signal time-dependent characteristics of second-harmonic Transferred Electron Oscillators (TEO's) and Heterostructure Barrier Varactor (HBV) frequency triplers have been obtained. This is accomplished by using a novel and efficient harmonic-balance circuit analysis technique which facilitates the integration of physics-based hydrodynamic device simulators. The integrated hydrodynamic device/harmonic-balance circuit simulators allow TEO and HBV circuits to be co-designed from both a device and a circuit point of view. Comparisons have been made with published experimental data for both TEO's and HBV's. For TEO's, excellent correlation has been obtained at 140 GHz and 188 GHz in second-harmonic operation. Excellent correlation has also been obtained for HBV frequency triplers operating near 200 GHz. For HBV's, both a lumped quasi-static equivalent circuit model and the hydrodynamic device simulator have been linked to the harmonic-balance circuit simulator. This comparison illustrates the importance of representing active devices with physics-based numerical device models rather than analytical device models.**

I. Introduction

THE design of diode sources operating in the 100–300 GHz range requires an efficient computer-aided design tool to calculate and optimize the power at all harmonics as a function of the device characteristics, embedding impedances of the circuit, and device packaging parameters. In order to accurately model the interactions between the active nonlinear device and the embedding circuit, a harmonic-balance circuit analysis is required. Similarly, to accurately calculate the large-signal time-dependent characteristics of the active device, a numerical hydrodynamic simulation of the electron transport in the device should be used. Commercially available harmonic-balance codes do not utilize a hydrodynamic treatment of the device due to the complexity of combining the two solution algorithms. Instead, a lumped quasi-static equivalent circuit analysis of the nonlinear device is typically employed to simplify the algorithm and aid in convergence. At high frequencies, however, accurately simulating the large-signal nonstationary high frequency dynamics of the electron transport via a hydrodynamic analysis is crucial; in the case of Transferred Electron Devices (TED's), it is the only means for accurately describing the large-signal dynamics of TED operation.

In this paper, we describe the simulation of 100–300 GHz harmonic sources using a novel harmonic-balance circuit analysis algorithm linked to hydrodynamic device simulators. In particular, we investigate second-harmonic Transferred Electron Oscillators (TEO's) and odd harmonic Heterostructure Barrier Varactor (HBV) frequency triplers. To facilitate the analysis, large-signal time-dependent numerical device simulators, with excellent computational speed and convergence properties, have been developed for GaAs and InP TED's [1], [2], as well as GaAs/InGaAs/AlGaAs on GaAs, InGaAs/InAlAs on InP, and InGaAs/InP on InP HBV's [3], [4]. The device simulations are based on numerical solutions of the first two moments of the Boltzmann Transport Equation coupled to Poisson's equation. For the TEO simulations, a detailed thermal analysis incorporating the chip and package parameters is included in the electron transport calculations. The harmonic-balance algorithm is a novel fixed-point voltage update scheme that allows the use of hydrodynamic device simulators in the large-signal analysis of nonlinear circuits [5].

II. Harmonic-Balance Circuit Analysis Technique

The novel harmonic-balance circuit analysis technique employed here is derived from the robust multiple-reflection algorithm [5], [6]. The time-domain current through the device active region is calculated by a hydrodynamic device simulator, for one period, as described separately in the next two sections for TED's and HBV's. The harmonic components of the current are extracted, using a discrete fourier transform, from the time-domain current waveforms produced by the hydrodynamic device simulators. The number of harmonics included in the analysis has been limited such that the chosen harmonics accurately reproduce all time-domain current waveforms being considered; for the HBV tripler simulations, thirteen harmonics have been considered, while six harmonics are considered for the TEO simulations. A fixed-point iterative expression [5] is then used to update the total voltage applied directly across the active region of the device in terms of the embedding impedances of the circuit, the harmonic components of the device current, and the harmonic components of the voltage from previous iterations. This iterative process continues until the harmonic components of the voltage converge to their steady-state values; intrinsic device impedances and output powers are calculated, at the harmonics of interest, once convergence is achieved. Complex

Manuscript received July 22, 1994; revised October 27, 1994. This work was supported by NSF Grant Nos. ECS-9113123 and ECS-9202037.

M. F. Zybura, J. R. Jones, and S. H. Jones are with the Department of Electrical Engineering, University of Virginia, Charlottesville, VA 22903 USA.

G. B. Tait is with the Department of Electrical Engineering and Computer Science, United States Military Academy, West Point, NY 10996 USA.

IEEE Log Number 9409118.

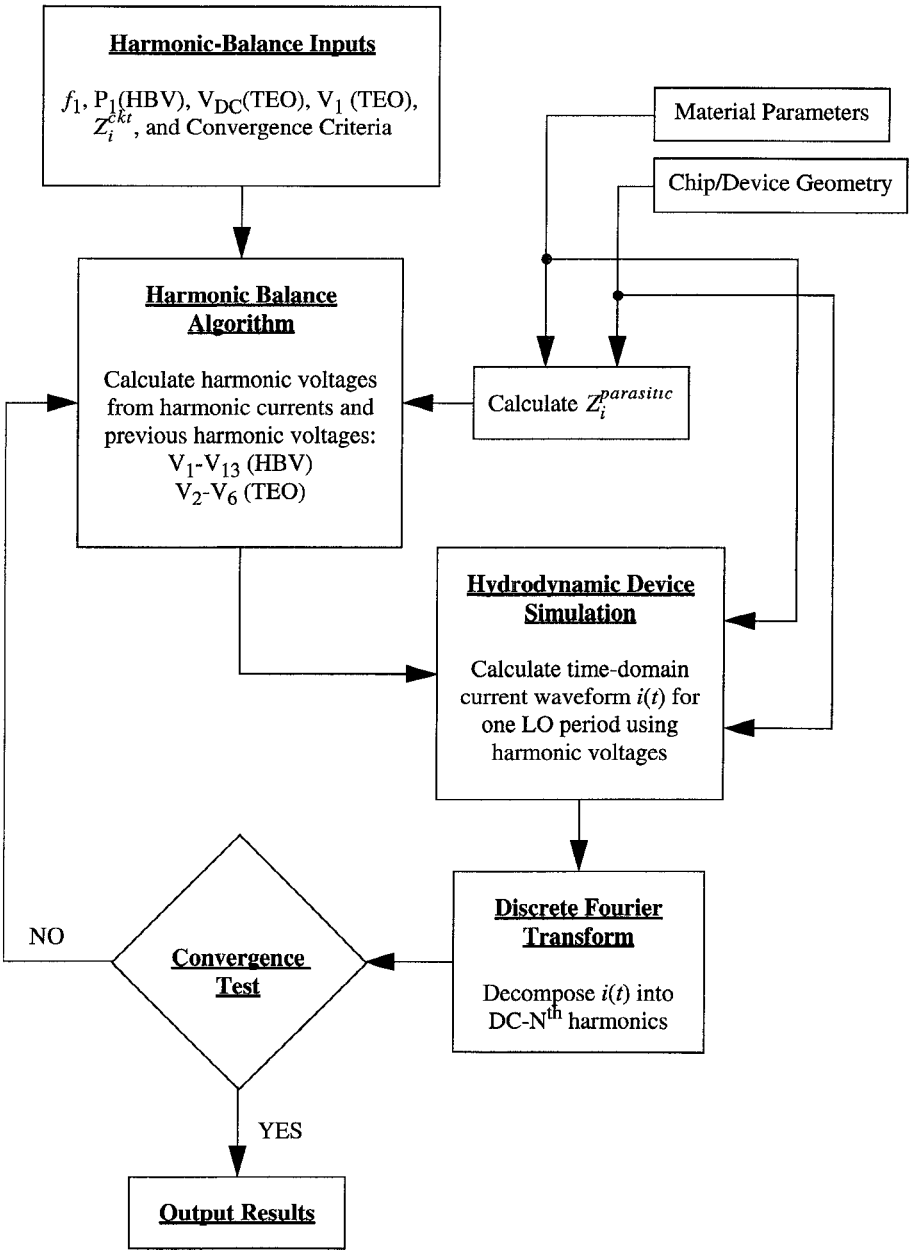

Fig. 1. Schematic representation of the integrated hydrodynamic device/harmonic-balance circuit solution algorithm.

frequency-dependent parasitic impedances, external to the active region of the device and similar to those of reference [6], are included in the analysis as additional contributions to the linear device embedding circuit. The power generated at each harmonic is, thus, calculated from

$$P = \frac{\mathcal{R}e(Z_d + Z_p)|I|^2}{2}, \tag{1}$$

where Z_d and Z_p are the harmonic device and parasitic impedances, respectively, and I is the total device current at a given harmonic. The entire hydrodynamic device/harmonic-balance circuit solution algorithm is shown schematically in Fig. 1. Again, the hydrodynamic device simulation block shown in this figure will be discussed separately for TEDs and HBVs as it is a device-specific portion of the entire analysis technique.

The novelty in the harmonic-balance algorithm utilized here is that, in deriving the fixed-point iterative voltage update expression, we use *a priori* knowledge, from Kirchhoff's voltage law, that the nonlinear device impedance (intrinsic device impedance plus parasitic device impedance) will equal the negative of the linear circuit impedance (embedding impedance) for each of the undriven harmonics in the steady state. This approach eliminates the computationally intensive and potentially unstable Runge-Kutta numerical time-integration necessary in the original multiple-reflection algorithm [6], and automatically calculates complex under-relaxation parameters for each harmonic component of the fixed-point iterative voltage update equation. More importantly, this approach explicitly provides the voltage applied across the active region of the device, facilitating the efficient

incorporation of physics-based numerical device models. In order to increase the computational speed and convergence properties of the harmonic-balance circuit analysis, a Steffenson numerical acceleration scheme for iterative equations, adopted from the secant methods of numerical analysis [7], is also utilized. Overall, a convergence rate nearly that of Newton-type methods is achieved, while the arduous tasks of constructing Jacobian matrices and solving large linear systems are avoided.

III. Second-Harmonic Transferred Electron Oscillator Simulation

A. Simulation Technique

The TED simulator used here is a modified version of a previously described simulation program [1], [2]. The hydrodynamic equations governing TED electron transport are the one dimensional continuity equation, the temperature dependent drift/diffusion equation, and Poisson's equation

$$\frac{\partial n(x,t)}{\partial t} = \frac{1}{q}\frac{\partial J_n(x,t)}{\partial x}, \tag{2}$$

$$J_n(x,t) = q\mu[\xi(x,t),T(x)]n(x,t)\xi(x,t) + qD[\xi(x,t),T(x)]\frac{\partial n(x,t)}{\partial x} + qn(x,t)D_n^T(x)\frac{dT(x)}{dx}, \tag{3}$$

and

$$\frac{\partial^2 \psi}{\partial x^2} = \frac{q}{\epsilon}[n(x,t) - N_D(x)], \tag{4}$$

where n, q, and J_n are the electron concentration, electron charge, and electron particle current density, respectively. In (2), ξ, μ, D, D_n^T, and T are the electric field, temperature- and field-dependent mobility and diffusivity, thermal diffusivity, and lattice temperature (assumed to be the same as the electron temperature), respectively. In (3), ψ is the electrostatic potential, ϵ is the dielectric permittivity of the device material, and N_D is the donor impurity concentration. These equations are discretized and solved using the half implicit Crank-Nicolson technique [8]. The lattice temperature in the device is sequentially calculated from a closed form solution to the heat equation for the packaged diode, where the heat generated in each region is determined from the fourier decomposed DC component of the device current [2]. The electron dynamics are more accurately simulated using temperature- and field-dependent mobility and diffusivity values that have been extracted from three-valley Monte Carlo simulations. Ohmic and fluid outflow boundary conditions are used at the cathode and anode of the device, respectively. The total device current is determined by

$$I = \frac{A}{l}\int_0^l J_n\, dx + \frac{\epsilon A}{l}\frac{dV}{dt}, \tag{5}$$

where A and l are the area and length of the device active region, respectively.

As indicated in Fig. 1, the fundamental operating frequency, DC bias, doping profile, and chip characteristics are adjustable inputs to the hydrodynamic device simulator; simulator outputs include time-domain voltage and current waveforms, electric field and electron concentration profiles versus time and position, and the temperature profile throughout the packaged device. The ac driving voltage is allowed to sweep over a range where peak power and stability are anticipated limiting optimization to the DC and fundamental driving voltages.

B. Results and Discussion

To demonstrate correlation between simulated and experimental results, comparisons have been made with the published experimental data of Rydberg [9] and Crowley *et al.* [10]. The InP TEO of reference [9] has a 1.1-μm active region, an active region doping profile graded from $1.4 \times 10^{16}\,\mathrm{cm}^{-3}$ at the cathode to $1.6 \times 10^{16}\,\mathrm{cm}^{-3}$ at the anode, and a 40–50 μm mesa diameter. Fig. 2 shows a surface contour of the simulated power generation versus circuit impedance for a domain of second-harmonic (188 GHz) circuit impedances in the range $1.55\,\Omega \le R_1 \le 10.55\,\Omega$ and $0.0\,\Omega \le X_2 \le 10.0\,\Omega$. Because the device is typically capacitive, only positive reactances have been considered. Six harmonics have been considered, and the circuit impedances of the higher harmonics (3rd–6th) have been set to 0.001 Ω for both the resistive and reactive components. Peak power generation of 6.4 mW is predicted for fundamental and second-harmonic circuit impedances of $Z_1^{ckt} = 0.8 + j6.6\,\Omega$ and $Z_2^{ckt} = 2.3 + j3.0\,\Omega$, respectively. Power generation of about 2 mW is expected for second-harmonic circuit impedances as large as $Z_2^{ckt} = 10 + j10\,\Omega$. Experimentally, Rydberg has demonstrated ~5 mW of generated power at 188 GHz in second-harmonic operation. Fig. 3 shows the simulated time-domain voltage waveform, as well as the particle, displacement, and total current waveforms for this device operating under peak second-harmonic power generation conditions. The associated electron concentration profiles for this device are shown in Fig. 4. Snapshots of the electron concentration are given in increments of one fifth of the fundamental period. As expected for n^+-n-n^+ type TED's at these frequencies, this device operates in an accumulation mode with the charge instabilities nucleating about 0.5 μm from the cathode. As the impressed voltage rises, accumulation layers form and reduce the total current; a phase shift is thus introduced between the total current and the voltage such that power generation is possible. The calculated temperature profile across the active region of this device increases from 412 K at the cathode to 443 K at the anode.

The n-n^+ TEO of reference [10] has a 1.8-μm active region doped at $1.1 \times 10^{16}\,\mathrm{cm}^{-3}$, and a 60 μm mesa diameter. At a fundamental frequency of 70 GHz and a DC bias of 9.0 V, the simulations predict peak power and stability for $V_{\mathrm{ac}} = 7.8$ V. This yields a fundamental circuit impedance of $Z_1^{ckt} = 0.3 + j11.7\,\Omega$. Since the fundamental frequency is cutoff and no power is generated or dissipated, the fundamental impedance is essentially reactive plus some small parasitic resistance. It is important to note that by reducing the total device chip thickness to 10 μm, the fundamental parasitic device resistance has been reduced to about 0.2 Ω [10]. The optimal second-harmonic circuit impedance is found to be

TABLE I
COMPARISON BETWEEN EXPERIMENT AND SIMULATION FOR DEVICES OF [9] AND [10] UNDER SECOND-HARMONIC OPERATION

Device	Second-Harmonic Frequency (GHz)	V_{DC} (V)	Z_2 (Ω)	I_{DC} (mA)	Power (mW)	η (%)
Rydberg	188	4.8	—	710	5	0.15
Simulation	188	4.0	-2.3-j 3.0	739	6	0.2
Crowley	140	9.0	—	222	47	2.3
Simulation	140	9.0	-4.7-j 6.0	281	40	1.5

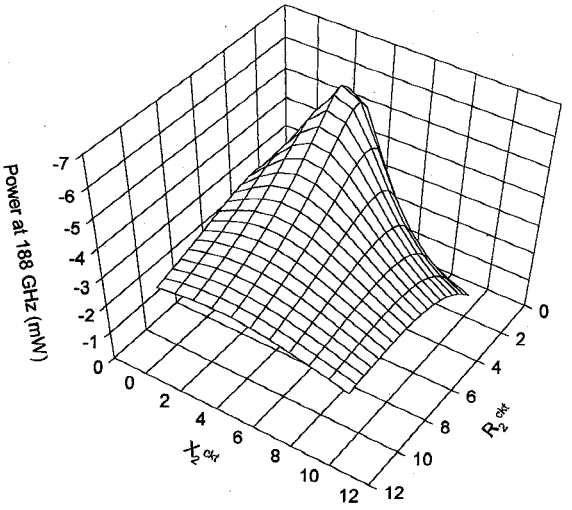

Fig. 2. Second-harmonic (188 GHz) power versus second-harmonic circuit impedances for the device of [9] with $V_{DC} = 4.0$ V, $V_{ac} = 2.0$ V, and $Z_2^{ckt} = 0.8 + j6.6\,\Omega$. Higher harmonic ($n \geq 3$) resistive and reactive components are set to 0.001 Ω.

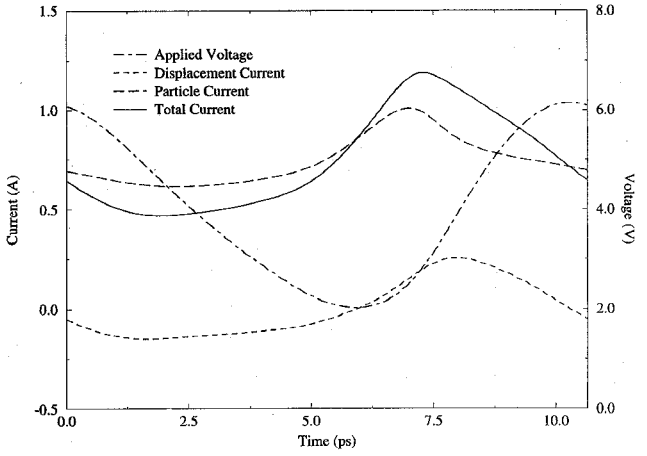

Fig. 3. Simulated voltage and current waveforms for the TED of [9] under second-harmonic operation.

$Z_2^{ckt} = 4.7 + j6.0\,\Omega$ yielding about 40 mW of generated power. Excellent load pulling characteristics are anticipated with this device since the second-harmonic component of the current waveform originates from the response of the nonlinear device to a large fundamental voltage. The simulated temperature for this device is 369 K at the cathode and 398 K at the anode. Overall, Table I shows comparisons of the experimental and simulated results for both devices under second-harmonic operation. Excellent correlation is observed

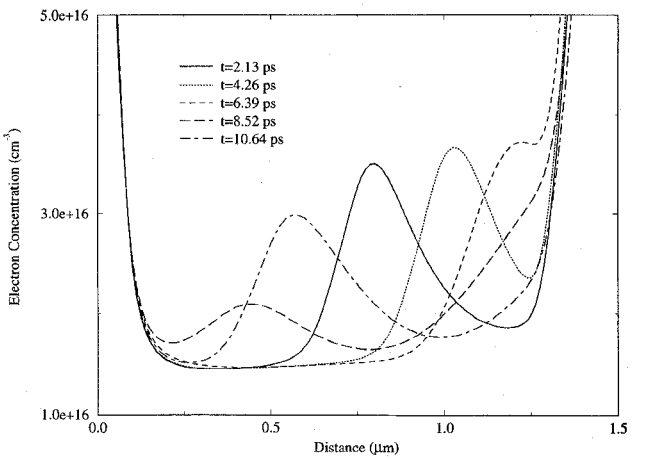

Fig. 4. Simulated second-harmonic (188 GHz) TED electron concentration versus time and position for the device of [9].

for both TEO circuits operating in second-harmonic mode, and similar results have been obtained from comparisons with reference [9] under third-harmonic (282 GHz) operation.

IV. HETEROSTRUCTURE BARRIER VARACTOR SIMULATION

A. Simulation Technique

The HBV simulator [3], [4] combines electron transport through the heterostructure bulk with electron transport across the abrupt heterointerfaces in a fully self-consistent manner. Carrier transport through the bulk regions of an HBV is described by the following set of one-dimensional, first-order coupled nonlinear differential equations for electrons

$$\frac{\partial n(x,t)}{\partial t} = \frac{1}{q}\frac{\partial J_n(x,t)}{\partial x}, \tag{6}$$

$$J_n(x,t) = -\frac{q^2 \tau_p(x) n(x,t)}{m^*(x)}\frac{\partial \phi_n(x,t)}{\partial x}, \tag{7}$$

$$D(x,t) = -\varepsilon(x)\frac{\partial \psi(x,t)}{\partial x}, \tag{8}$$

and

$$\frac{\partial D(x,t)}{\partial x} = -q[n(x,t) - N_D(x)], \tag{9}$$

where

$$n(x,t) = n_{i,\mathrm{ref}} \exp\left[\frac{q}{kT}(\psi(x,t) + V_n(x) - \phi_n(x,t))\right]. \tag{10}$$

J_n is the electron particle current density, n is the electron concentration, ϕ_n is the electron quasi-Fermi potential, ψ is the electrostatic potential, D is the electric displacement, k is Boltzmann's constant, q is the electron charge, T is the absolute temperature, $n_{i,\mathrm{ref}}$ is the intrinsic electron density in the reference material (GaAs or InP), and V_n, τ_p, m^*, N_D, and ϵ are the spatially-dependent alloy potential [11], momentum relaxation time, electron conductivity effective mass, donor impurity concentration, and dielectric permittivity, respectively. Electron transport across the abrupt heterointerfaces of an HBV is described by a set of one-dimensional nonlinear electron particle current density equations which take into account thermionic emission and thermionic-field emission of carriers over and through the abrupt barrier [12]. Regardless of bias polarity, one of the two heterointerfaces in a single barrier HBV is biased above flat-band; to account for this, we have utilized the semiconductor-semiconductor heterointerface analog [3], [4] to the boundary constraint of Adams and Tang [13], [14] for metal-semiconductor interfaces at high forward bias.

The simulation technique employed for HBVs differs slightly from that outlined for TED's. In particular, Poisson's equation is reduced to two first-order differential equations ((8) and (9) instead of (4)), and the state variable set J_n, ϕ_n, ψ, and D is utilized instead of J_n, n, and ψ. This solution approach facilitates the accurate and efficient simulation of electron transport through the heterostructure bulk combined with electron transport across the abrupt heterointerfaces [12]. Overall, the carrier transport equations are solved, in the three regions (one barrier and two modulation) of the device, at a given bias value, and subject to the heterointerface constraints and ideal ohmic contact boundary constraints, via the coupled equation Newton-Raphson method. As indicated in Fig. 1, HBV alloy composition and doping profiles, and chip geometry are adjustable inputs to the hydrodynamic device simulator; simulator outputs include time-domain voltage and current waveforms, particle and displacement components of the total device current, and electric field and electron concentration profiles versus time and position.

B. Results and Discussion

Excellent correlation has been obtained between the HBV hydrodynamic device simulator and experimental DC I–V and static C–V characteristics. Fig. 5 shows the experimental DC I–V and static C–V characteristics of the Choudhury *et al.* whisker-contacted single barrier GaAs/AlGaAs HBV's [15]; also shown in this figure are simulated characteristics from the HBV hydrodynamic device simulator and curve-fits to the simulated characteristics. The Choudhury *et al.* devices have active regions consisting of 213 Å intrinsic $Al_{0.7}Ga_{0.3}As$ barriers surrounded by 53 Å intrinsic GaAs spacer layers and 5330 Å n-type ($1 \times 10^{17}\,\mathrm{cm}^{-3}$) GaAs modulation layers. The measured parasitic resistance of 7.0 Ω has been utilized in calculating the simulated and curve-fit DC I–V and static C–V characteristics. The slight asymmetry evident in the experimental Choudhury *et al.* data has been modelled via a slight asymmetry in the modulation layer

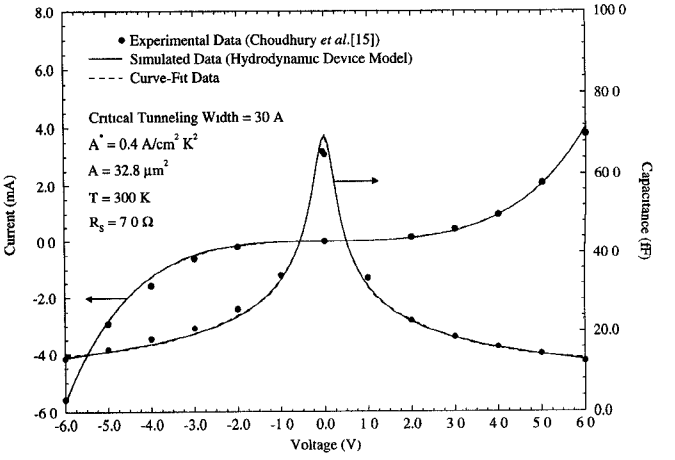

Fig. 5. Experimental, simulated, and curve-fit DC I–V and static C–V characteristics for the single barrier $GaAs/Al_{0.7}Ga_{0.3}As$ HBV's of [15].

doping concentrations; one side of the device is assumed to have a doping concentration of $1.0 \times 10^{17}\,\mathrm{cm}^{-3}$, while the other side is assumed to have a doping concentration of $1.125 \times 10^{17}\,\mathrm{cm}^{-3}$. The simulated C–V characteristics have been obtained by calculating the change in charge with respect to the change in applied bias, for sufficiently small bias steps, on the depletion or accumulation side of the device.

For comparison purposes, the harmonic-balance circuit analysis technique has been combined with both the HBV hydrodynamic device simulator and a simple quasi-static analytical HBV device model derived from the HBV hydrodynamic device simulator. The quasi-static analytical HBV device model utilizes curve fits to the device DC I–V and static C–V characteristics as obtained from the HBV hydrodynamic device simulator so that the total device current as an instantaneous function of bias $i(V(t))$ is

$$i(V(t)) = I_{\mathrm{DC}}(V(t)) + C_{\mathrm{Static}}(V(t))\frac{dV}{dt}. \qquad (11)$$

Both HBV harmonic-balance simulation approaches have been compared to the Choudhury *et al.* experimental results for a GaAs/AlGaAs HBV frequency tripler operating near 200 GHz. The device parasitic impedances have been calculated, similar to reference [6], using estimated chip parameters (ohmic contact resistivities of $2 \times 10^{-6}\,\Omega\,\mathrm{cm}^2$, substrate thickness of 4 mil, and square chip side lengths of 250 μm) and the mesa parameters given in [15] for the n^+ epitaxial layers external to the active region. The calculated DC parasitic resistance of 7.07 Ω compares favorably with the measured value of 7.0 Ω quoted in reference [15]. The calculated fundamental and third-harmonic parasitic impedances are $8.01 + j0.99\,\Omega$ and $8.73 + j1.72\,\Omega$, respectively. At the incident pump powers of interest, near-optimum fundamental and third harmonic circuit impedances have been estimated from [15] for a device parasitic resistance of 7.0 Ω. For simulation purposes, the remaining circuit impedances have been set to short-circuit impedances of $0.001 + j0.0\,\Omega$.

The steady-state time-domain voltage and current waveforms, obtained from both simulation approaches for a 64 GHz, 20 mW incident pump signal, are compared in Fig. 6. The associated electron concentration profiles, obtained from

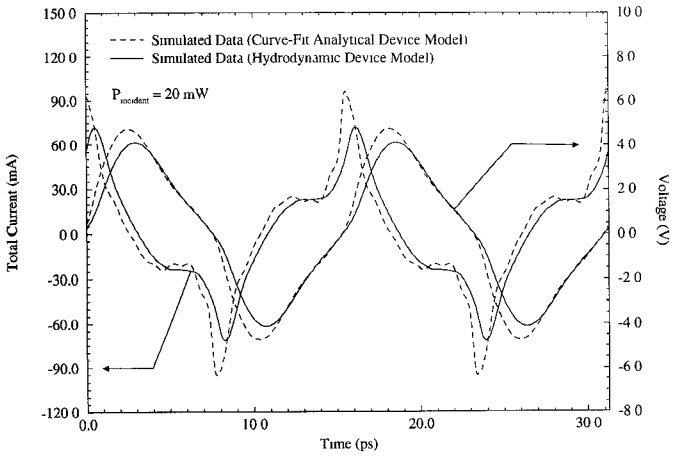

Fig. 6. Simulated steady-state harmonic-balance voltage and current waveforms, for the single barrier $GaAs/Al_{0.7}Ga_{0.3}As$ HBV's of [15], obtained using both analytical and hydrodynamic device models. Incident pump power is 20 mW at a pump frequency of 64 GHz.

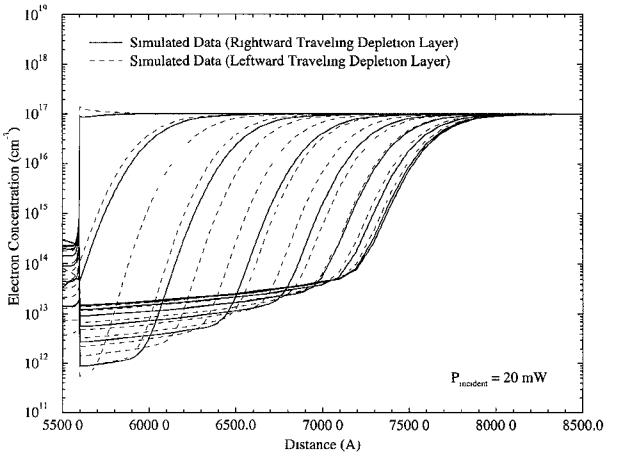

Fig. 7. Simulated electron concentration versus time and position over the depletion side of the single barrier $GaAs/Al_{0.7}Ga_{0.3}As$ HBV's of [15] for half of a steady-state LO cycle. Incident pump power is 20 mW at a pump frequency of 64 GHz. Electron concentration snapshots are taken at increments of one fortieth of the fundamental period (approximately every 0.39 ps).

the hydrodynamic device simulator for half of a steady-state LO cycle and over the depletion side of the device, are shown in Fig. 7. The electron concentration snapshots are taken at increments of one fortieth of the fundamental period. The fundamental and third-harmonic circuit impedances used to obtain these results are $Z_1^{ckt} = 13.0 + j75.0\,\Omega$ and $Z_3^{ckt} = 14.0 + j25.75\,\Omega$, respectively. Although the two sets of voltage and current waveforms have the same general shape, the sharpness, magnitudes, and phases of the waveforms differ substantially. As a result, the predicted absorbed power, third harmonic output power, and tripling efficiency are substantially overestimated by the analytical device/harmonic-balance circuit simulator. This can be seen clearly in Fig. 8 which shows the experimental tripling efficiency versus incident pump power for the Choudhury *et al.* HBV's, along with the results obtained from both harmonic-balance simulation approaches. The simulated results given in this figure are the maximum predicted efficiencies as they change very little with small variations in the fundamental and third-harmonic circuit impedances estimated from [15]. At an incident pump power of 20 mW, the analytical device/harmonic-balance circuit simulator predicted an absorbed power of 18.7 mW and a third-harmonic output power of 3.24 mW (tripling efficiency of 17.4%) as compared to an absorbed power of 19.2 mW and a third harmonic output power of 1.69 mW (tripling efficiency of 8.77%) for the hydrodynamic device/harmonic-balance circuit simulator. The intrinsic device efficiency was estimated in [15] to be about 4.2%. From these results, it is apparent that the time-dependent behavior of electrons in HBV's is not adequately accounted for using a simple analytical device model in conjunction with the harmonic-balance circuit analysis. The dynamic high frequency nonstationary behavior of the carriers is clearly modelled more accurately by a full numerical device model incorporating hydrodynamic transport equations. The use of the harmonic-balance circuit analysis technique presented here facilitates such a modeling approach.

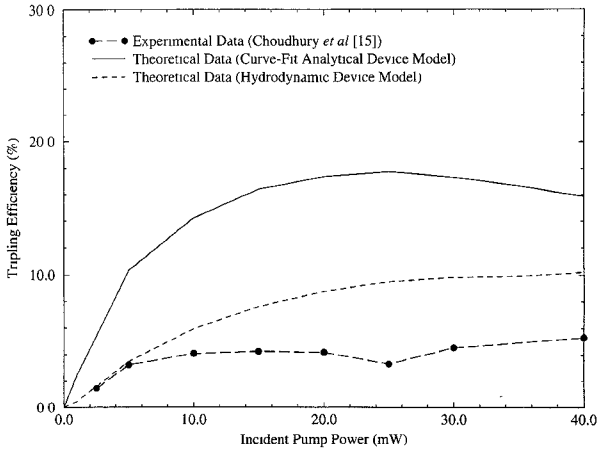

Fig. 8. Experimental and simulated tripling efficiencies versus incident pump power for the single barrier $GaAs/Al_{0.7}Ga_{0.3}As$ HBV's of [15] subject to 64 GHz pump excitation.

V. Conclusion

In conclusion, accurate and efficient simulations of the large-signal time-dependent characteristics of TEO and HBV circuits have been obtained by combining a novel harmonic-balance circuit analysis technique with physics-based hydrodynamic device simulators. For TEO's, the use of a hydrodynamic device simulator is the only means for accurately describing the large signal dynamics of TED operation. Comparisons between our hydrodynamic device/harmonic-balance circuit simulator has yielded excellent correlation for InP TEO's operating at 140 and 188 GHz. In the case of HBV's, where a simple lumped quasi-static equivalent circuit of the diode can be developed, the dynamic high frequency nonstationary behavior of carriers in the device is not adequately modelled by such a device model. Instead, improved correlation between experimental and simulated results has been obtained using a hydrodynamic device model

in conjunction with the harmonic-balance circuit analysis technique. The integrated hydrodynamic device/harmonic-balance circuit analysis technique described here, therefore, allows highly nonlinear circuits, such as TEO's and HBV's, to be co-designed from both a circuit and a device point of view.

ACKNOWLEDGMENT

J. R. Jones is supported by a USAF Laboratory Graduate Fellowship under the sponsorship of the Solid-State Directorate, Wright Laboratory, WPAFB, OH. The authors thank J. E. Carlstrom of the California Institute of Technology, T. W. Crowe of the University of Virginia, and N. R. Erickson of the University of Massachusetts for stimulating technical discussions relevant to this work.

REFERENCES

[1] M. F. Zybura, S. H. Jones, and G. B. Tait, "Efficient computer aided design of second-harmonic GaAs and InP millimeter wave TEDs," in *Proc. Int. Semiconductor Device Res. Symp.* Charlottesville, VA, Dec. 1–3, 1993, pp. 775–778.

[2] ——, "Efficient computer-aided design of GaAs and InP millimeter wave transferred electron devices including detailed thermal analysis," *Solid-State Electron*, vol. 38, no. 4, pp. 873–880, April 1995.

[3] J. R. Jones, G. B. Tait, and S. H. Jones, "DC and large-signal AC electron transport properties of GaAs/InGaAs/AlGaAs heterostructure barrier varactors," in *Proc. 1993 Int. Semiconductor Device Res. Symp.* Charlottesville, VA, Dec. 1–3, 1993, pp. 389–392.

[4] ——, "DC and large-signal time-dependent electron transport in heterostructure devices: An investigation of the heterostructure barrier varactor," to appear in *IEEE Trans. Electron Dev.*, vol. 42, no. 6, June 1995.

[5] G. B. Tait, "Efficient solution method for unified nonlinear microwave circuit and numerical solid-state device simulation," *IEEE Microwave and Guided Wave Lett.*, vol. 4, no. 12, pp. 420–422, Dec. 1994.

[6] P. H. Siegel, A. R. Kerr, and W. Hwang, "Topics in the optimization of millimeter-wave mixers," NASA Tech. Paper No. 2287, Mar. 1984.

[7] J. Ortega and W. Rheinboldt, *Iterative Solution of Nonlinear Equations in Several Variables*. New York: Academic, 1970.

[8] G. B. Tait and C. M. Krowne, "Efficient transferred electron device simulation method for microwave and millimeter wave CAD applications," *Solid-State Electron.*, vol. 30, no. 10, pp. 1025–1036, Oct. 1987.

[9] A. Rydberg, "High efficiency and output power from second- and third-harmonic millimeter wave InP-TED oscillators at frequencies above 170 GHz," *IEEE Electro. Dev. Lett.*, vol. 11, no. 10, pp. 439–441, Oct. 1990.

[10] J. D. Crowley, C. Hang, R. E. Dalrymple, D. R. Tringali, F. B. Fank, L. Wandinger, and H. B. Wallace, "140 GHz indium phosphide Gunn diode," *Electron. Lett.*, vol. 30, no. 6, pp. 499–500, Apr. 1994.

[11] M. S. Lundstrom and R. J. Schuelke, "Numerical analysis of heterostructure semiconductor devices," *IEEE Trans. Electron. Dev.*, vol. 30, no. 9, pp. 1151–1159, Sept. 1993.

[12] G. B. Tait and C. R. Westgate, "Electron transport in rectifying semiconductor alloy ramp heterostructures," *IEEE Trans. Electron Dev.*, vol. 38, no. 6, pp, 1261–1270, June 1991.

[13] J. Adams and T. W. Tang, "A revised boundary condition for the numerical analysis of Schottky barrier diodes," *IEEE Electron Dev. Lett.*, vol. 7, no. 9, pp. 525–527, Sept. 1986.

[14] ——, "Computer simulation of boundary conditions for Schottky barrier diodes," *Electron. Lett.*, vol. 25, no. 16, pp. 1098–1100, Aug. 1989.

[15] D. Choudhury, M. A. Frerking, and P. D. Batelaan, "A 200 GHz tripler using a single barrier varactor," *IEEE Trans. Microwave Theory Tech.*, vol. 41, no. 4, pp. 595–599, Apr. 1993.

Michael F. Zybura was born in Carapito, Venezuela, in 1966. He received the B.S. degree in physics from the University of Maryland, College Park, MD, in 1989, and the M.S. degree in electrical engineering from the University of Virginia, Charlottesville, VA, in 1992.

He is currently working toward the Ph.D. degree in electrical engineering as a research assistant at the University of Virginia, Charlottesville, VA, where his present interests include semiconductor device physics and modelling, and nonlinear microwave and millimeter wave circuit analysis and design.

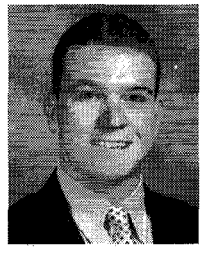

J. Robert Jones (S'89) was born in Trenton, NJ, in 1968. He received the B.S. and M.S. degrees in electrical engineering from the University of Virginia, Charlottesville, VA, in 1990 and 1992, respectively.

He is presently working toward the Ph.D. degree in electrical engineering at the University of Virginia, Charlottesville, VA, where he has been a research assistant since 1989. His current research interests include semiconductor heterostructure device physics and modeling, and nonlinear microwave and millimeter wave circuit analysis and design.

Mr. Jones is a member of Tau Beta Pi and Eta Kappa Nu.

Stephen H. Jones (S'84, M'89) was born in Medfield, MA, in 1962. He received the B.S., M.S., and Ph.D. degrees in electrical engineering from the University of Massachusetts, Amherst, MA, in 1984, 1987, and 1989, respectively.

He joined the faculty of the Department of Electrical Engineering at the University of Virginia, Charlottesville, VA in 1989. His current research interests include electronic device fabrication, and millimeter wave device design and simulation for frequency multipliers and oscillators.

Dr. Jones is an officer of the National Capital Section of the Electrochemical Society, the Central Virginia Joint Chapter of the IEEE Microwave Theory and Techniques and IEEE Electron Device Societies, and the International Semiconductor Device Research Symposium.

Gregory B. Tait (A'83–S'83–M'84–S'86–M'90) was born in Holyoke, MA, in 1960. He received the B.A. degree in physics from Amherst College, Amherst, MA, in 1982, the M.S. degree in electrical engineering from the University of Maryland, College Park, MD, in 1984, and the Ph.D. degree in electrical engineering from Johns Hopkins University, Baltimore, MD, in 1991.

From 1982 to 1986, he was a member of the technical staff in the Advanced Communications Department at Fairchild Communications and Electronics Company, Germantown, MD. From 1986 to 1994, he conducted research at the Microwave Technology Branch of the Electronics Science and Technology Division, Naval Research Laboratory, Washington, DC. Additionally, he served as an adjunct faculty member of the Department of Electrical Engineering at the University of Virginia, Charlottesville, VA, from 1992 to 1994. In 1994, he joined the faculty of the Department of Electrical Engineering and Computer Science at the United States Military Academy, West Point, NY. His current research interests include semiconductor heterostructure device physics, nonlinear microwave circuits, and high temperature superconducting microwave filters.

Dr. Tait is a member of Phi Beta Kappa, Sigma Xi, URSI Commission D, and the American Physical Society. (For a photograph of Dr. Tait, see p. 1601 of the Sept. 1994 issue of this TRANSACTIONS.)